An Investigation on the Damping Ratio of Marine Oil Slicks in Synthetic Aperture Radar Imagery

Cornelius Quigley, A. Malin Johansson, *Member, IEEE*, and Cathleen E. Jones, *Member, IEEE*

***Abstract*—The damping ratio has recently been used to indicate the relative internal oil thickness within oil slicks observed in synthetic aperture radar (SAR) imagery. However, there exists no well-defined and evaluated methodology for calculating the damping ratio. In this study, we review prior work regarding the damping ratio and outline its theoretical and practical aspects. We show that the most often used methodology yields damping ratio values that differ, in some cases significantly, for the same scene. Three alternative methods are tested on multifrequency datasets of verified oil slicks acquired from DLR's F-SAR instrument, NASA's unmanned aerial vehicle synthetic aperture radar, and Sentinel-1. All methods yielded similar results regarding relative thickness variations within slick. The proposed damping ratio derivation methods were found to be sensitive to the proportion of oil covered pixels versus open water pixels in the azimuth direction, as well as to the scene size in question. We show that the fully automatable histogram method provides the most consistent results even under challenging conditions. Comparisons between optical imagery and derived damping ratio values using F-SAR data show good agreement between the relatively thicker oil slick areas for the two different types of sensors.**

***Index Terms*—Damping ratio (DR), oil slick, oil spill response, optical, synthetic aperture radar (SAR).**

I. Introduction

SYNTHETIC aperture radar (SAR) has become a key operational tool for the detection and surveillance of mineral oil slicks in the marine environment. Although radar has long been used for mapping the spatial extent of oil spills [1], methods for quantifying the internal characteristics of an oil slick, such as the variation in slick thickness, are not widely adopted by operational services. Current methods to determine the thickness variations of oil slick rely heavily on methods such as the Bonn Agreement Oil Appearance Codes (BAOAC) for aerial observers of oil slicks [2] and require optical imagery or visual survey. Major drawbacks to such methods are that they are subjective in nature, do not provide a wide-scale, synoptic assessment of the state of a slick, and are only applicable to new slicks assumed to not have undergone weathering. In SAR imagery, marine surface slicks are detectable by the smoothing of the ocean surface, which reduces the radar backscatter in comparison to the surrounding ocean. The viscoelastic properties of the marine slick material act to damp the capillary and short gravity waves via a decrease in surface tension and a reduction in wind friction [3]. For SAR imagery, the damping ratio (DR) can be used for extracting information relating to the internal, relative thickness of an oil slick [4], [5], [6], [7], [8], [9]. The DR measures the contrast between the radar backscatter of pixels within a slick and the surrounding ocean expressed as

$$\mathrm{DR}_{TR} = \frac{\sigma^{0,\mathrm{sea}}_{TR}(\theta)}{\sigma^{0}_{TR}(\theta)}. \tag{1}$$

Here, σ^0_{TR} is the normalized radar cross section (NRCS) of the entire SAR image for the transmit (T) and receive (R) polarimetric channels of the radar (TR will denote either the VV or HH polarimetric channels for the purpose of this study), θ is the incidence angle, and $\sigma^{0,\mathrm{sea}}_{TR}$ is the radar cross section from clean, open water external to the oil slick, which needs to be estimated.

The DR is calculated from one copolarimetric channel only and is simple to interpret [10]. The DR is an emerging methodology that can be adopted by oil spill responders to aid in decision making [8]; therefore, having a robust derivation method is essential. However, there is little consensus or details within the literature on how to calculate $\sigma^{0,\mathrm{sea}}_{TR}(\theta)$. In addition, for several cases where a methodology is proposed, the proposed method can lead to ambiguities depending on the specifics of how it is calculated, and these ambiguities could lead to the misidentification of high priority areas within slick for oil spill recovery. This is especially true when techniques involving time-series data are considered in conjunction with the DR [11].

In this study, we aim to evaluate the methods for calculating the DR and identify those that can be readily applied to a wide variety of oil spill scenarios and which can produce nonvarying numerical results. Specifically, this study is designed to demonstrate strengths and weaknesses for the different methods examined. We also examine the methods' capability of identifying zones of thicker oil within a slick.

To meet this end, a detailed literature review is provided in Section II to illustrate the experimental and theoretical aspects of the DR, as well as outlining the primary method for calculating $\sigma^{0,\mathrm{sea}}_{TR}(\theta)$ proposed in the literature to date. In addition, Section III outlines new and recently proposed methods for calculating $\sigma^{0,\mathrm{sea}}_{TR}(\theta)$. Section IV describes the data used to evaluate the

Manuscript received 6 March 2023; revised 17 May 2023; accepted 7 June 2023. Date of publication 12 June 2023; date of current version 26 June 2023. This work was supported in part by CIRFA and the Research Council of Norway under Grant 237906 and in part by the Jet Propulsion Laboratory, California Institute of Technology, under contract with the National Aeronautics and Space Administration. *(Corresponding author: Cornelius Quigley.)*

Cornelius Quigley and A. Malin Johansson are with the Department of Physics and Technology, UiT–The Arctic University of Norway, NO-9037 Tromsø, Norway (e-mail: cornelius.p.quigley@uit.no; malin.johansson@uit.no).

Cathleen E. Jones is with Jet Propulsion Laboratory, California Institute of Technology, Pasadena, CA 91125 USA (e-mail: cathleen.e.jones@jpl.nasa.gov).

Digital Object Identifier 10.1109/JSTARS.2023.3285145

methods. Section V compares the DR results derived using the different methods. Section VI provides a comparison of the DR to corresponding optical imagery. Section VII concludes the article.

II. Damping Ratio

This section provides an overview of the literature regarding the DR derived from SAR imagery as well as the proposed methods to calculate it. Experiments using scatterometer data are also discussed as the resulting conclusions are applicable to SAR data. Studies that address the DR from a purely theoretical perspective and that are more model based, or where the DR is investigated under highly controlled settings (such as laboratory wave tank experiments), are not considered in this review. For a thorough discussion on these aspects of the DR, the interested reader is referred to [12], [13], [14], [15], [16], [17], [18], [19], [20], [21], and [22]

Section II-B summarizes the methods for calculating the DR [particularly the $\sigma_{TR}^{0,\text{sea}}$ part of (1)] that have been presented in the cited literature.

A. Prior Work

Some of the cardinal work investigating the reduction of radar backscatter from the ocean surface, in the presence of surface-dwelling marine slicks, was conducted in the German Bight using the helicopter mounted 5-frequency/multipolarization scatterometer, HELIcopter SCATerometer (HELISCAT) [5]. The mission was flown for the purposes of acquiring data in Ku-, X-, C-, S-, and L-bands for four substances, which were simultaneously released. The authors of that study found that under all wind conditions encountered, the measured DR increased with increasing Bragg wavenumber, and the DR decreases with increasing wind speed. These conclusions are also supported by the authors in [4], [6], and [23] using spaceborne and airborne X-, C-, and L-bands imagery.

The wind direction was also found to affect the DR through the radar look direction, with an upwind-downwind asymmetry between the wave amplitude profiles and the radar backscatter [6]. They concluded that this is probably due to the influence of wind direction on the wave peaks. This finding was supported by Skrunes et al. [24], where, using UAVSAR time series data collected during the NOrwegian Radar oil Spill Experiment 2015 (NORSE 2015), they found that the DR values were higher when the sensor was looking downwind compared to upwind.

In [9], the DR was found to be higher for heavy fuel than for light fuel oil spills at Ku-, X-, C-, and S-bands, while at L-band, DR values were the same across all scattering surfaces. In addition, the authors of [25] concluded that the copolarization DR is the preferable method for assessing internal zones of variable thickness over polarimetric decomposition parameters, such as entropy due to noise corruption, particularly in the HV channel. Minchew et al. [6] showed that there is a small dependence of the DR upon polarization, with the VV polarization channel showing a higher degree of damping than the HH.

The authors of [23] and [26] advocate for the use of X-band SAR as a means of detecting mineral oil in SAR imagery, arguing that the DR values are higher in the X-band than at other frequencies and, thus, increase the likelihood of slick detection. Similarly, Skrunes et al. [27] report that even very low volume oil discharges (0.001%–0.002%) were clearly detectible in X-band imagery via the DR. However, in [27], they also outline limitations due to noise corruption of X-band instruments arising from the low SNR, and as a result, they advocate for the use of C- and L-bands SAR systems due to their better noise characteristics.

B. Damping Ratio as Presented in the Literature

Even though many studies rely on the DR, the past literature (with the exception of [10] which will be discussed in Section III) fails to explicitly provide a cogent methodology for calculating $\sigma_{TR}^{0,\text{sea}}(\theta)$. In [5], [6], [9], [23], [25], and [26], no explanation for calculating $\sigma_{TR}^{0,\text{sea}}(\theta)$ was provided. Studies that reference the DR and which provide a methodology for calculating $\sigma_{TR}^{0,\text{sea}}(\theta)$ include [4], [8], [24], [27], and [11]. These studies cite the same basic method, herein referred to as *the strip method,* which can be summarized as follows and is depicted in Fig. 1(a).

Given an image in radar coordinates (azimuth $\times$ slant range), a strip of undefined pixel height in the azimuth direction and extending across the scene in the slant range direction is extracted from a clean ocean area somewhere in the scene, preferably adjacent to the slick. It should be stated that the authors in [26] used a strip with 800 pixels in the azimuth direction. The values are averaged in the azimuth direction. While they do not state a reason for choosing that amount, it is assumed that they choose an amount sufficient to get an accurate average value for $\sigma_{TR}^{0,\text{sea}}(\theta)$. This yields a profile vector that has the same length as the dimension of the image in the slant range direction. This profile vector then acts as an unsmoothed estimate for $\sigma_{TR}^{0,\text{sea}}(\theta)$, where the slant range pixel number maps to the incidence angle. Although it is not explicitly stated in [8], [11], [24], and [27], the authors of those studies then apply a polynomial fit to the averaged profile to derive a smoothed estimate for $\sigma_{TR}^{0,\text{sea}}(\theta)$ [28]. This is a necessary step as averaged open water pixel values can still show significant variation as a function of incidence angle and if the fit is not used, then discontinuities can show up in the DR map.

One issue with this method is that it assumes that the oil slick is self-contained within the image, making it possible to find a single sufficiently wide strip of clean water crossing the scene. A further issue is that this method can lead to ambiguities in the returned DR values depending on the portion of the image the strip is taken from, particularly when the NRCS of clean water varies across the scene as is common in coastal areas.

III. Methods Proposed for Calculating the Damping Ratio

In Section II-B, we demonstrated that there is one primary method presented in the past literature for calculating the DR. In this section, we consider three alternative methods that can also be utilized for determining the DR.

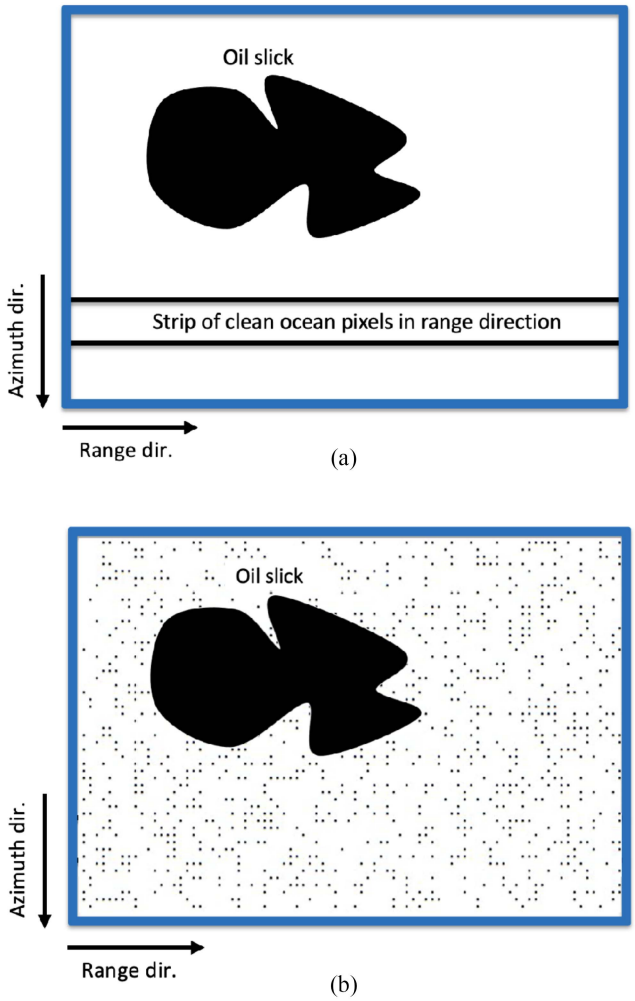

Fig. 1. Setup showing (a) strip method and (b) random sampling method. The randomly selected pixels are marked as black dots in (b). A polynomial fit is applied to the resulting profile, which is derived from the sampled pixels, and acts as an estimate for $\sigma_{TR}^{0,\text{sea}}(\theta)$. For the random sampling method, the oil slick needs to be identified and masked out before this operation is carried out.

One characteristic of the strip method is that it estimates $\sigma_{TR}^{0,\text{sea}}(\theta)$ by utilizing a sample of the open water pixels present within a scene, which presupposes that the slick has been identified so that it is excluded from the sample. Here, we propose an alternative method that is implemented under the same assumption, referred to as the *random sampling method*. This involves masking out the oil-slicked areas of the image and then randomly selecting open water pixels in the azimuth direction for each point in the range direction. In this study, the masks separating the oil infested areas from open water were manually created. The randomly selected pixels are then averaged, resulting in a profile that has a length the same as the scene in the range direction. A polynomial fit is again applied to the resulting profile. This setup can be seen in Fig. 1(b). It should be noted that applying the strip and random sampling methods can be difficult. This is due to the complexity of identifying and masking out oil pixels as well as finding open ocean pixels covering the full incidence angle range.

We also investigate two additional methods that utilize all pixels within a scene to estimate $\sigma_{TR}^{0,\text{sea}}(\theta)$.These two methods are referred to as the *median method* and the *histogram method* [10].

The median method relies on taking the median of all pixels in the azimuth direction (encompassing both slick and open water) for each point in the range direction. The reasoning behind this method is that there should be many more open water pixels than oil infested pixels so that the median can act as an indicator for the backscatter in oil free areas, yet not be sensitive to outliers within the scene such as ships and oil rigs. As with the previous two methods outlined, a polynomial fit is then applied to the median derived profile. Further information on estimating the DR using this method can be found in [29].

The histogram method, described in detail in [10], uses all the pixels in the scene to separate clean water from radar-dark areas. It relies on the fact that clean water has higher intensity returns than slicks to identify "high confidence" clean water pixels, which are then used to calculate the numerator in (1) $\sigma_{TR}^{0,\text{sea}}(\theta)$. The method requires that a mask is applied to remove land if present in the scene because land can be significantly brighter than clean water. The method is shown schematically in Fig. 2, which shows the histogram for a scene with a clean water peak (higher σ values, peak on right) and a peak comprised mainly of pixels from the slick (lower σ values, peak on left). High confidence clean water pixels are selected as those with σ values near the center of the clean water peak, and their average used as the estimate for $\sigma_{TR}^{0,\text{sea}}(\theta)$. The algorithm was found to work well when pixels within the full-width-half-maximum were used, but the results were insensitive to exact limits, and this can be a tunable parameter. For scenes where the incidence angle varies by more than a few degrees, the scene is separated into incidence angle bins and the method applied to each bin's pixels, then a polynomial fit is performed to obtain $\sigma_{TR}^{0,\text{sea}}(\theta)$. In practice, bin sizes of 1°–2° work well. The DR map is then calculated by applying (1) to all pixels in the scene.

The histogram method has advantages particularly for extensive and distributed oil slicks, and because it uses all pixels in the scene, it is fully automatable. It is insensitive to outliers from ships, rigs, or near-shore structures such as wharves because they show up in the high intensity tail of the clean water peak whose values are not used in calculating $\sigma_{TR}^{0,\text{sea}}(\theta)$. The scene can be mostly oil-covered water if there are sufficient clean water pixels to have an identifiable peak in the histogram. Because the method does not require the slick to cover only a small fraction of the scene, the user can elect to crop the scene to better capture local conditions when there are fronts elsewhere in the scene. In addition to working for the 2-peak scenario depicted in Fig. 2, the method works if there are more than two peaks, e.g., mineral oil with high damping and low wind areas with moderate damping in addition to clean water, because the peak with highest σ value is identified as clean seawater, and it also works when there is only one peak, e.g., oil slicks with returns that fall within the low-intensity tail of the clean water peak.

It should be noted that the four methods cited in this study can be applied to georeferenced scenes provided an incidence angle map is available.

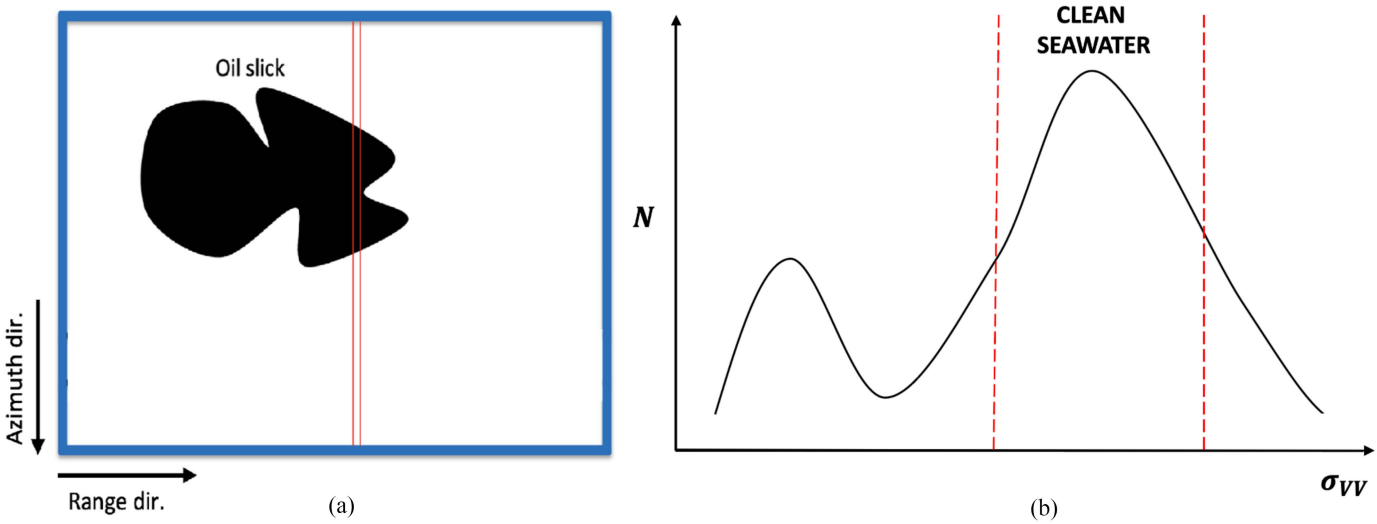

Fig. 2. Methodology for determining the DR using the histogram method [10]. (a) Diagram showing a SAR image of an oil slick with open water pixels shown in white. The space between the two red vertical lines indicates the incidence angle bin that will be considered. (b) Histogram of VV-intensity values for the pixels in the incidence angle bin subtended by the two red lines in (a). Clean water shows up as a peak with the highest intensity values. An average of pixels around the peak (between solid lines) is taken to estimate the NRCS for clean water in this incidence angle bin. This is done for all angle bins. A polynomial fit is applied to retrieve $\sigma_{TR}^{0,\text{sea}}(\theta)$.

IV. Data

The following sections provide a brief overview of the datasets used in this study and the instruments used to acquire them, which include F-SAR, UAVSAR, and Sentinel-1.

A. F-SAR Dataset From NORSE 2019

The F-SAR data were acquired during the NORSE 2019 as an embedded part of the Norwegian Clean Seas Association for Operating Companies (NOFO) oil-on-water campaign [30]. Information about F-SAR is found in Table I, and the reader is directed to [31] for more information about the instrument. The experiment was conducted in the North Sea (N 59° 59', E 2° 27') on June 12, 2019, with wind speeds of 12 m/s. During the campaign, 26 separate quad-polarimetric acquisitions in X-, S-, and L-bands were made over the course of two flights, imaging both mineral oil emulsion and soybean oil, which were used as a biogenic slick simulator [30].

One of the acquisitions from flight 2 is used in this study, with the S-band image featured in Fig. 3(a), where both the mineral oil emulsion and the soybean oil slick can be seen. The "head" of the mineral oil slick, i.e., the portion of the slick with the highest oil concentration and which is located directly downwind, is highlighted by a red box. In the following analysis, we focus solely on the mineral oil slick. Fig. 3(b) shows a photograph taken from inside the Dornier DO228-212 aircraft that housed the F-SAR instrument. As can be seen, the head of the slick is thicker than the tail due to its higher solar reflectivity and brighter appearance. Visual observations of the head of the mineral oil slick from the research vessel R/V Helmer Hanssen indicated the oil had a discontinuous true oil color. This corresponds to oil slick with a thickness range of 50–200 μm according to the BAOAC [2].

Notably, there are significant differences in the location of thick/dense material in the two discharged slicks, in relation to wind direction. As seen in Fig. 3(a), the mineral oil slick exhibits dark radar pixels more in the downwind area, while the soybean oil slick shows them more in the upwind area. This is likely due to differences in 3-D transport between biogenic oil and mineral oil caused by their distinct depth profiles. Jones et. al. [34] found that a discharged monomolecular biogenic film was entrained more quickly and mixed much deeper into the water column than discharged mineral oil emulsion and, despite the small droplet size, resurfaced to maintain an observable slick, showing that very small droplets are not necessarily dispersed below the surface. A similar phenomenon may explain the differences observed in the F-SAR data, indicating that soybean oil may be less influenced by wind compared to mineral oil.

B. UAVSAR Dataset From the Santa Barbara Campaign

The second dataset used in this study was acquired off the coast of Santa Barbara, California, on May 12, 2021 and imaged the Coal Oil Point seep field. A total of 12 images were acquired over a 4-h period, with one of the later images shown in Fig. 4.

The UAVSAR instrument is a left-looking L-band SAR mounted on a Gulfstream-III aircraft. The radar is fully polarimetric, with a range bandwidth of 80 MHz (2 m range resolution) and a range swath of 22 km, corresponding to an incidence angle range of ~17°–67°. For ocean applications, the scene is cropped in the near range (25°) to be more sensitive to surface roughness and in the far range (62°) to avoid low signal-to-noise ratio. Relevant sensor information is given in Table I.

This acquisition represents a "real-world" coastal ocean oil spill scenario where the oil slick is dispersed throughout the scene, has an irregular shape, consists of many disconnected slicks, and is present at every incidence angle. In addition, land

TABLE I
PROPERTIES OF SAR DATA ACQUISITIONS AND COINCIDENT *IN SITU* INFORMATION

	Acquisition from NORSE 2019 (F-SAR)	**Acquisition from Santa Barbara (UAVSAR)**	**Acquisition from Mediterranean Sea (Sentinel-1A)**
Time (UTC) and date of acquisitions	11:42 12 June 2019	18:58 12 May 2021	05:28 8 Oct. 2018
Incidence angle range of mineral oil emulsion slick [°]	43.8 - 59.1	25.0–62.0 (entire scene)	40.4–41.6
Platform type	Airborne	Airborne	Spaceborne
Sensor velocity [m/s]	90.4	209.0	N/A
Sensor altitude [m]	2456.6	12495.7	N/A
Flight direction (Cardinal dir. and dir. relative to wind)	Southwest (Upwind)	Northwest (Downwind)	N/A
Pass direction	N/A	N/A	Descending
Sensing mode	N/A	N/A	IW
Approx. age of emulsion at time of acquisition [hours]	6.0	<12	~ 24
Amount of oil discharged onto ocean surface [m^3]	2	Unknown (natural seep)	Unknown
Wind speed [m/s]	12.0	3.8 – 4.8	Unknown
Pixel spacing (Slant Rg × Az) [m]	X-band: (0.60 × 0.18) S-band: (0.60 × 0.18) L-band: (0.60 × 0.36)	L-band: (6.18 × 6.18)	C-band: (2.3 × 14.1)§
Frequency of radiation [GHz]	X-band: 9.60* S-band: 3.25 L-band: 1.33	L-band: 1.26‡	C-band: 5.41§
Noise Equivalent Sigma Zero (NESZ) [dB] (near Rg, minimum, far Rg)	X-band: -38.0, -45.0, -29.0† S-band: -34.5, -47.0, -40.5 L-band: -48.0, -57.1, -54.5	L-band: -40.2, -47.0, -39.0‡	C-band: < -23.7§ (nominal)

(unless otherwise stated, information relating to SAR data sets taken from header files).
* Values for F-SAR taken from [31].
† F-SAR NESZ information computed in-house by DLR.
‡ Values for UAVSAR taken from [32].
§ Values for Sentinel-1 taken from [33].

is present but masked out using a land mask. In such complex, real-world cases, bathymetry, coastal currents, and direct land effects such as wind shadowing can make tracking oil slicks more difficult.

C. Sentinel-1 Data From Ship Collision in Mediterranean Sea

On October 8, 2018 at 05:28 UTC, a C-band Sentinel-1 satellite image was acquired of an oil spill resulting from a collision between two ships that had occurred the previous day in the Mediterranean Sea north of Corsica. This acquisition, as seen in Fig. 5, shows the discharged oil slick, which is approximately 20 km in length. Sensor information available in Table I.

In this study, we use this dataset to test the dependence on scene size for the four methods cited in Section III, i.e., we aim to test if the same DR values can be derived by using information contained within successively larger bounding boxes indicated with the red, green, and black regions of interest (ROIs) in Fig. 5. The shaded, rectangular segments below each box show the pixels that were used to calculate the DR using the strip method. The sizes for each of the ROIs are 300 × 300, 440 × 440, and 600 × 600 pixels, respectively. This includes the portions that are shaded in. The heights of the shaded portions are approximately a sixth the height of the corresponding bounding box, e.g., 50, 73, and 100 pixels for the red, green, and black shaded portions, respectively.

V. RESULTS OF METHOD COMPARISON

In Section V-A, we compare retrieval methods using the strip method and the random sampling method for the F-SAR data. These two methods are the first to be evaluated as they rely on determining $\sigma_{TR}^{0,\text{sea}}(\theta)$ using a portion of the open water pixels present within a scene.

In Section V-B, we test the random sampling, median, and histogram methods to determine if they can accurately identify variations in oil thickness within the slick. The strip method is omitted in this section due to conclusions drawn from Section V-A.

In Section V-C, we compare DR values retrieved using the median and histogram methods for the UAVSAR Santa Barbara dataset. These two methods are tested in this section because they are more applicable to a real-world operational setting in that they do not require preprocessing to identify the slick.

In Section V-D, we test the impact of scene size for all four methods previously outlined using the Sentinel-1 dataset.

A. Comparison Between Strip Method and Random Sampling Method for F-SAR Dataset

Fig. 6 shows the S-band F-SAR acquisition from the NORSE 2019 campaign, comprised of data with an angle of incidence of 35° or greater. Incidence angles less than 35° are not

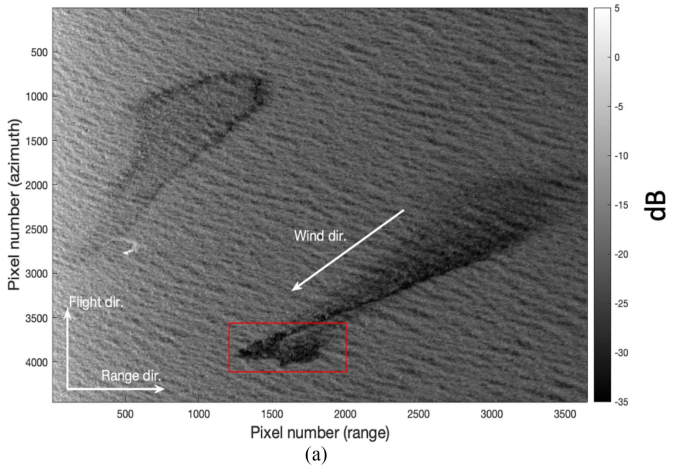

(a)

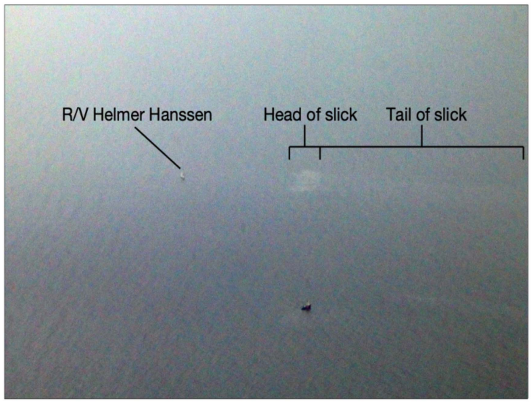

(b)

Fig. 3. (a) S-band F-SAR intensity image (σ^0_{VV}) in range-Doppler coordinates multilooked by a 9 × 9 window acquired at 11:42 UTC. The "head" of the mineral oil slick is downwind of the rest of the slick and contains most of the oil (red box). The soybean oil slick (biogenic slick simulator) can be seen in the upper left portion of the image. (b) Photograph of mineral oil slick taken from Dornier DO228-212 aircraft carrying the F-SAR instrument at 11:46 UTC. The "head" of the slick can be observed as being thicker in contrast to the "tail" of the slick. Photograph: Ralph Horn. Images published with permission from NOFO.

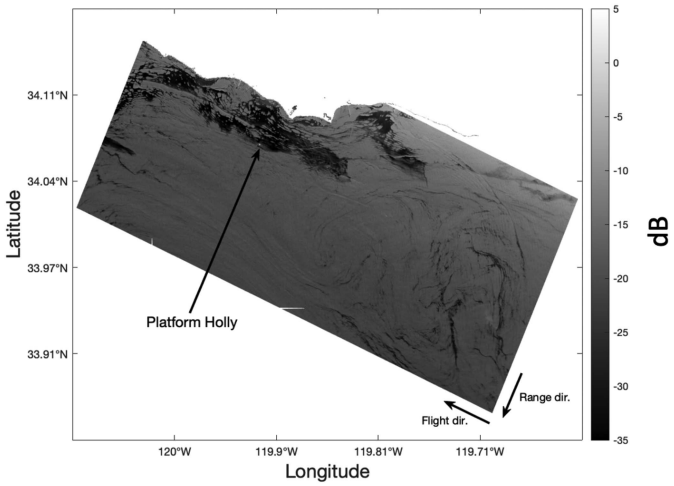

Fig. 4. Georeferenced L-band UAVSAR intensity image, which is multilooked by a 3 × 12 window. Scene shows a natural oil slick seep off the coast of Santa Barbara, California. The land areas have been masked out in the image.

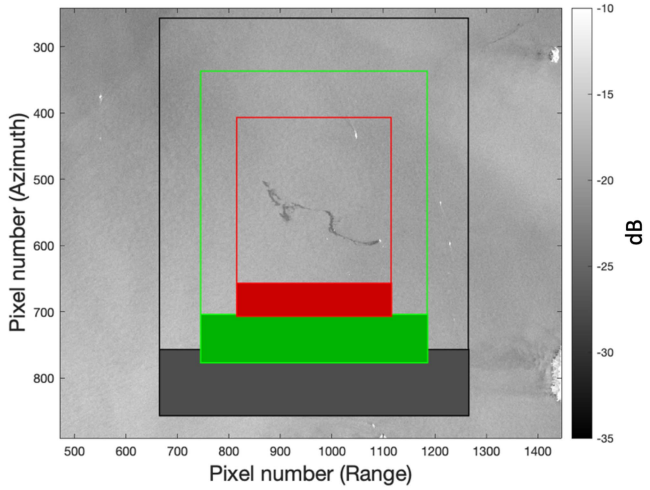

Fig. 5. C-band Sentinel-1 intensity image (σ^0_{VV}) multilooked by a 9 × 9 window. The spill occurred north of the island of Corsica. Different scene extents used to evaluate the sensitivity to scene size selection are indicated by the red, green, and black boxes. Areas used to determine the clean sea NRCS for the strip method are indicated by the shaded regions.

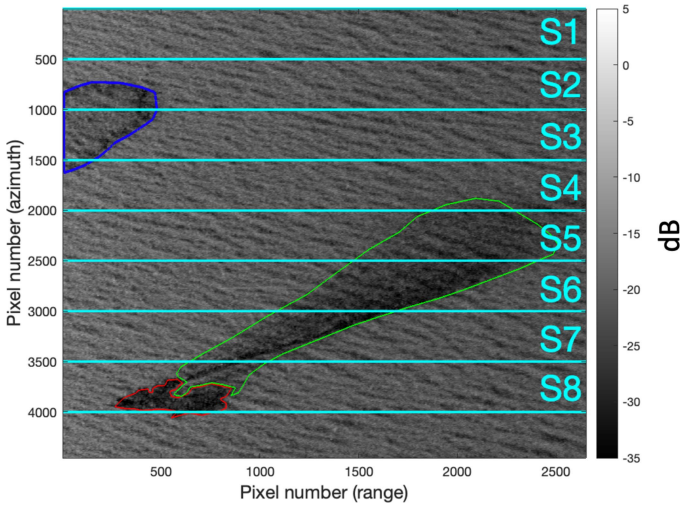

Fig. 6. Same as in Fig. 3(a) but only the areas with an angle of incidence of 35° and above are shown and will be considered in this section. The "head" of the slick is outlined in red, and the "tail" in green. The strips for which the DR will be calculated using the strip method are shown and are labeled from S1 to S8.

considered because the radar is relatively insensitive to small-scale roughness below this threshold [6], [35], [36]. The "head" of the slick is outlined in red, while the "tail" of the slick is outlined in green. The red and green boundaries were manually determined. In the following analysis, these two portions of the slick will be considered separately, and the DRs are derived for all three F-SAR frequency bands.

Also shown in Fig. 6 are eight strips, labeled from S1–S8, each 500 pixels in pixel height. Strips with a pixel height of 500 pixels were chosen to produce more strips for comparison. For each of the eight strips, the DR was calculated for both the "head" and the "tail." As can be seen, some of the strips overlap with the mineral oil slick as well as the portion of the plant oil slick outlined in blue. Therefore, some portions of the strips are

either missing open water pixels entirely or have less than 500 open water pixels in the azimuth direction. For the following analysis, only those portions of the strips that have 500 pixels in the azimuth direction are utilized. This results in gaps in the averaged profiles for which polynomial fits predict the missing values in these gaps.

While estimating $\sigma_{TR}^{0,\text{sea}}(\theta)$ using the random sampling method, only pixels that are external to the slicks, which are bound by the red, green, and blue curves, are considered. In total, $\sigma_{TR}^{0,\text{sea}}(\theta)$ is calculated by sampling 500 pixels randomly at each slant range bin. This was done once, i.e., no iterations performed. Fig. 7(a), (c), and (e) shows the mean of the 8 $\sigma_{TR}^{0,\text{sea}}(\theta)$, profiles derived using the strips S1–S8, as a solid black line for all three frequency bands. The standard deviation from the mean is indicated by the gray shaded regions. The derived $\sigma_{TR}^{0,\text{sea}}(\theta)$ profiles, calculated using the random sampling method (RS method) for all three frequency bands, are also plotted, and displayed as red dotted curves. As can be seen, the random sampling $\sigma_{TR}^{0,\text{sea}}(\theta)$ is generally close to the average of the eight-strip method-derived $\sigma_{TR}^{0,\text{sea}}(\theta)$ profiles.

Fig. 7(b), (d), and (f) shows the corresponding DR calculated using the RS method $\sigma_{TR}^{0,\text{sea}}(\theta)$ profiles for all three frequency bands. DR values were higher in S-band than in L-band, which agrees with theory and mirrors results presented by the authors in [4], [5], and [9]. However, some DR values derived from the X-band image were found to be lower than the S-band DR results. This is believed to a result of noise corruption and will be explored more in Section VI.

As expected, for all DR imagery displayed in Fig. 7(b), (d), and (f), the head of the slick displays higher DR values than the tail of the slick. Given that the tail of the slick is assumed to be composed mostly of silver sheen, its thickness is estimated to be 0.04–0.3 μm from the BAOAC [2]. As 2 m^3 of mineral oil emulsion were discharged, the average thickness of the head of the slick was determined to be 151–153 μm assuming all the released oil remained on the surface. This falls into the BAOAC discontinuous true oil color category [2]. As can be seen, the oil thickness estimated in the head is 3–4 orders of magnitude larger than the tail while the DR values for the head of the slick are at most 1 order of magnitude larger than the tail. This shows that the DR does not scale linearly with its physical counterpart.

To evaluate the likelihood that the strip method DR values provide similar results for different iterations, i.e., choosing a different specific location for each strip, the following analysis was performed. Each of the eight DR images, expressed as I_1, …, I_8, are subtracted from the other to construct a series of difference images, each of which shows the numerical difference in the DR values between iterations.

The difference images are given mathematically as $d_{xy} = I_x - I_y \ \forall \ x \neq y$, where $x, y \in [1], [8]$. This results in 28 difference images being created. Values from each of the 28 difference images are plotted together as a histogram.

Fig. 8(a) and (b) shows the histograms from the head and tail, respectively, of the slick for the X-, S- and L-bands with their standard deviations shown in the inserts. For the strip method, the standard deviations are on the order of 10^0–10^{-1}, indicating that DR values obtained using different strips vary significantly.

Interestingly, the standard deviation for the histograms calculated using the strip method tends to decrease as the radar frequency decreases for both the head and tail of the slick. This seems to suggest that the differences in the DR values derived using the strip method are greater for high-frequency bands than for low-frequency bands. One explanation for this decrease in standard deviation may be due to the varying effect of wind strength on the ocean surface across the scene. Wind has a greater impact on shorter capillary waves which correspond to surface waves with Bragg wavelengths responsible for backscatter at higher sensing frequencies. Thus, wind gusting may make the returned backscatter to the sensor more variable for higher frequencies (X-band) than lower frequencies (L-band). This is indicated in Fig. 7(a) and (e), where the standard deviation about the mean is greater for X-band than for L-band.

Fig. 8(c) shows an increase with increasing radar frequency in the mean DR, μ, of all strips for both the head and tail of the mineral oil slick. As can be seen, the DR values in the head of the mineral oil slick (thicker oil) tend to increase as the frequency of sensing radiation increases. In contrast, for the tail of the slick, the DR is roughly the same across all sensing frequencies. This aligns with the work presented in [9], who found that the gradient in a least square fit to DR values across scatterometer data covering frequencies from S- to Ku-bands was less for lighter fuel oils compared to heavy fuel oils. In the L-band DR estimates, the values are similar to the whole slick, in agreement with Wismann et al. [9], who found no difference in DR values for light and heavy fuel oils at L-band.

In conclusion, the strip method has a high degree of variability and is not considered in Section V-B or V-C.

B. Comparison Between Relative DR Values for Random Sampling, Median, and Histogram Methods for F-SAR Dataset

In Section I, it was stated that the DR is a viable measure for deriving information related to the relative thickness variations within an oil slick. In this section, we compare the ability of the random sampling, median, and histogram methods to accurately determine similar relative thickness variations within the slick.

In the following analysis, we compute the correlation coefficient and the slope of the regression line between combinations of the three proposed methods. These combinations include the histogram method versus random sampling method (HM versus RSM), the median method versus random sampling method (MM versus RSM), and the median method versus histogram method (MM versus HM). This is done for both the head and the tail of the mineral oil slick, for all three frequencies, and the results are normalized.

Table II lists the calculated slopes for the regression lines, where all three methods preserve the relative DR values between them. In addition, the correlation coefficients are 1 for all cases. This indicates that all three methods can determine the same information regarding the relative thickness of the oil slick. All three methods appear to show the greatest agreement between derived relative DR values in L-band with nearly all calculated slope values being closest to 1 for both the head and tail of the slick.

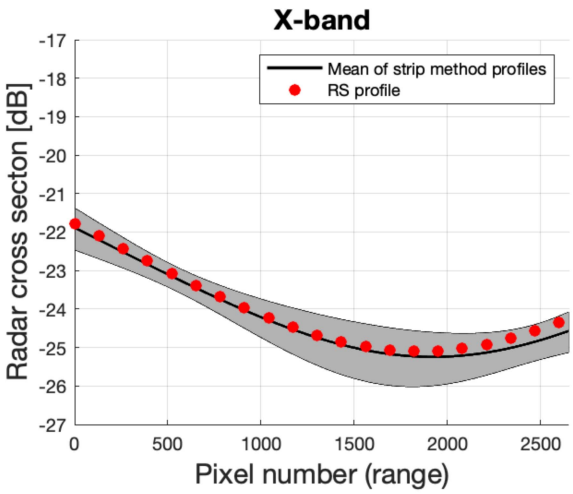

(a)

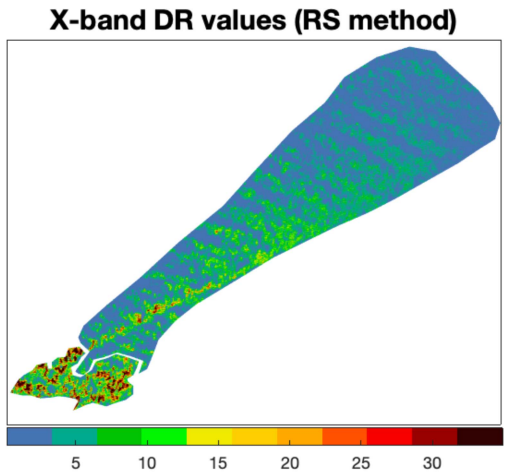

(b)

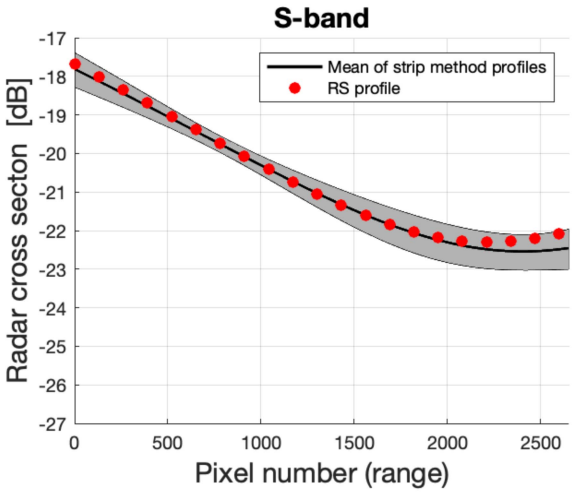

(c)

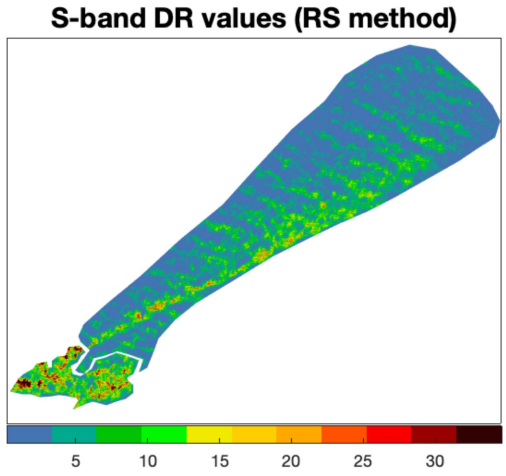

(d)

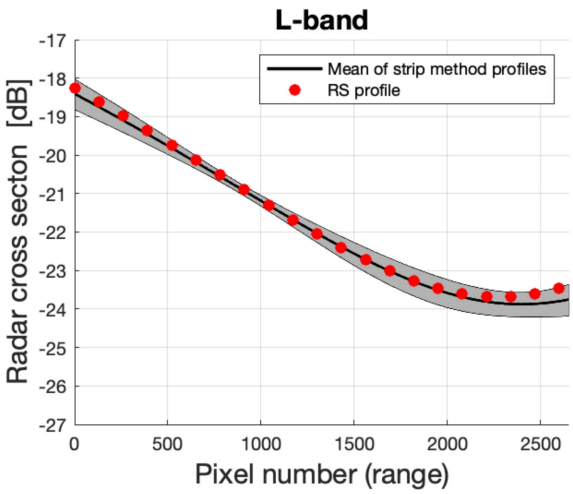

(e)

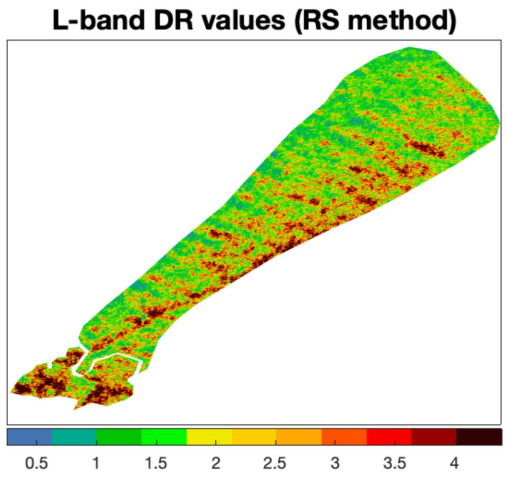

(f)

Fig. 7. (a), (c), (e) Solid black line indicates the mean for all eight derived $\sigma_{TR}^{0,\text{sea}}(\theta)$ profiles, calculated from open water, using the strip method (strips S1–S8) for all three frequency bands, respectively. The shaded gray regions indicate the standard deviation away from the mean. The red, dotted curve indicates the derived $\sigma_{TR}^{0,\text{sea}}(\theta)$ profiles calculated using the random sampling method (RS method) for all three frequency bands, respectively. (b), (d), (f) Corresponding DR imagery for both the head and tail of the slick calculated using the RS method.

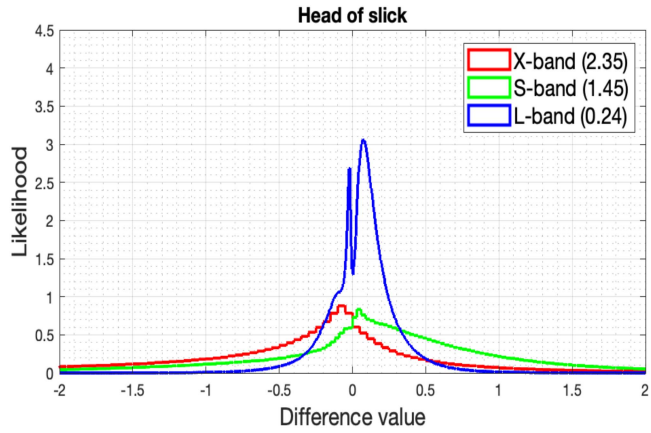

(a)

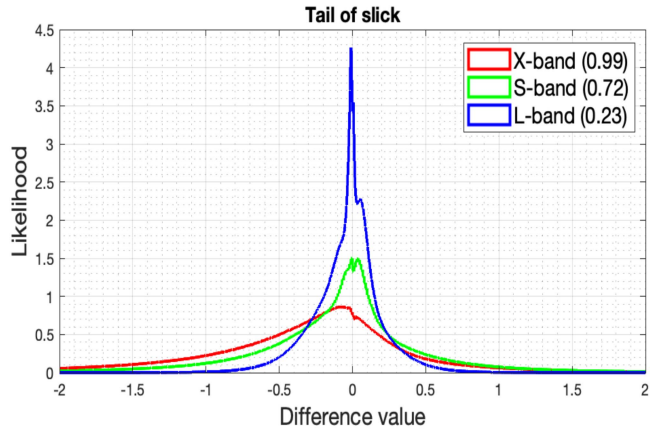

(b)

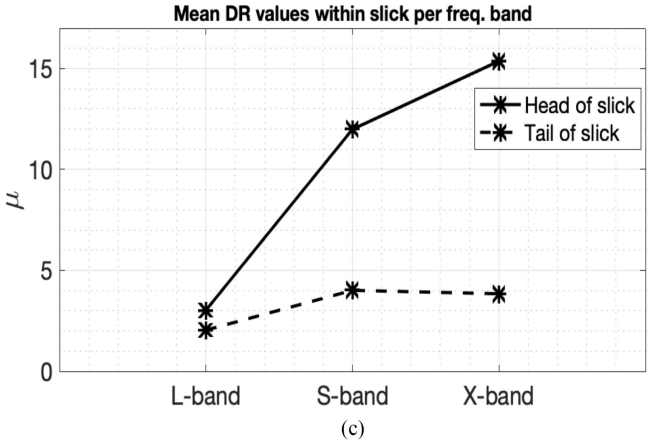

(c)

Fig. 8. (a), (b) Normalized histograms for 28 difference images for both the head and tail of the mineral oil slick in Fig. 6. The numbers in the legends indicate the standard deviation of the distributions. (c) Graph showing an increase in the mean μ of all strip method derived DR images $I_1, \ldots, I_8$ for both the head and tail of the mineral oil slick, with increasing sensing frequency.

When the three proposed methods show minimal differences between relative DR values, the corresponding differences between absolute DR values are not necessarily minimal also. Fig. 9 shows the normalized histograms for absolute difference values between methods for the head of the slick in L-band. As can be seen, the peaks are all less than 0.5 units in value. When working with time series data, these discrepancies could compound to produce errors in derived products. The smallest discrepancy between absolute DR values occurs between the histogram method and median method (yellow curve in Fig. 9) for this frequency band. As these two methods can be applied automatically and are more appropriate for real-world scenarios, they will be investigated further in Section V-C.

TABLE II
SLOPES FOR THE REGRESSION LINES BETWEEN DR RETRIEVAL METHODS

	Slopes for head of slick			Slopes for tail of slick		
	HM versus RSM	MM versus RSM	MM versus HM	HM versus RSM	MM versus RSM	MM versus HM
X-band	0.99	1.00	0.97	1.01	1.03	0.98
S-band	1.00	1.03	0.97	1.06	1.06	1.00
L-band	0.99	1.01	0.99	0.99	1.00	1.00

Not shown are correlation values that were 1 in every case.

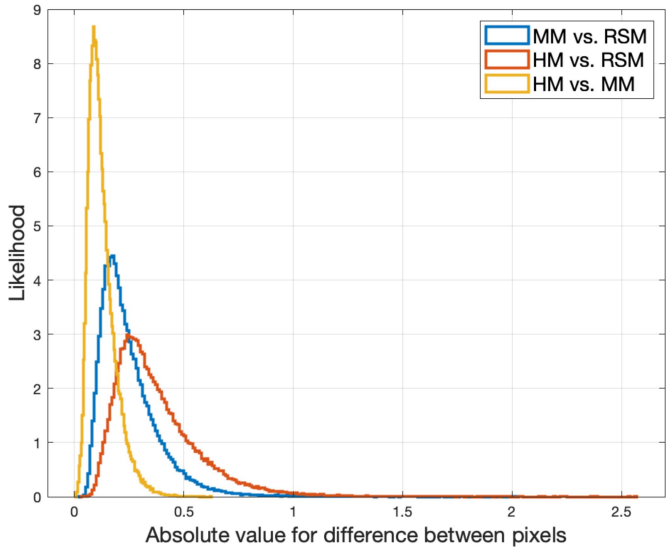

Fig. 9. Normalized histograms showing difference between derived DR values for the head of the mineral oil slick in L-band between various methods.

C. Comparison Between Retrieved DR Values for Median and Histogram Methods for Santa Barbara Dataset

Here, we test if the histogram method and median method show the same preservation in absolute DR values for the UAVSAR scene as for the F-SAR dataset. Fig. 10(a) shows the absolute difference between the two methods, where the largest differences are found in the slick areas closest to land (the masked-out portion of the image). These slicks are elongated and primarily oriented in the azimuth direction, close to land and occupy 30%–40% of the pixels in the azimuth direction.

We argue that the DR is underestimated when using the median method due to the high number of oil pixels in the $\sigma_{TR}^{0,\text{sea}}(\theta)$ estimate, which biases the result toward low clean sea NRCS values.

To support our argument, 50 ROIs with a size of 25×25 pixels were sampled from the oil slicks across the image. The ROIs (in

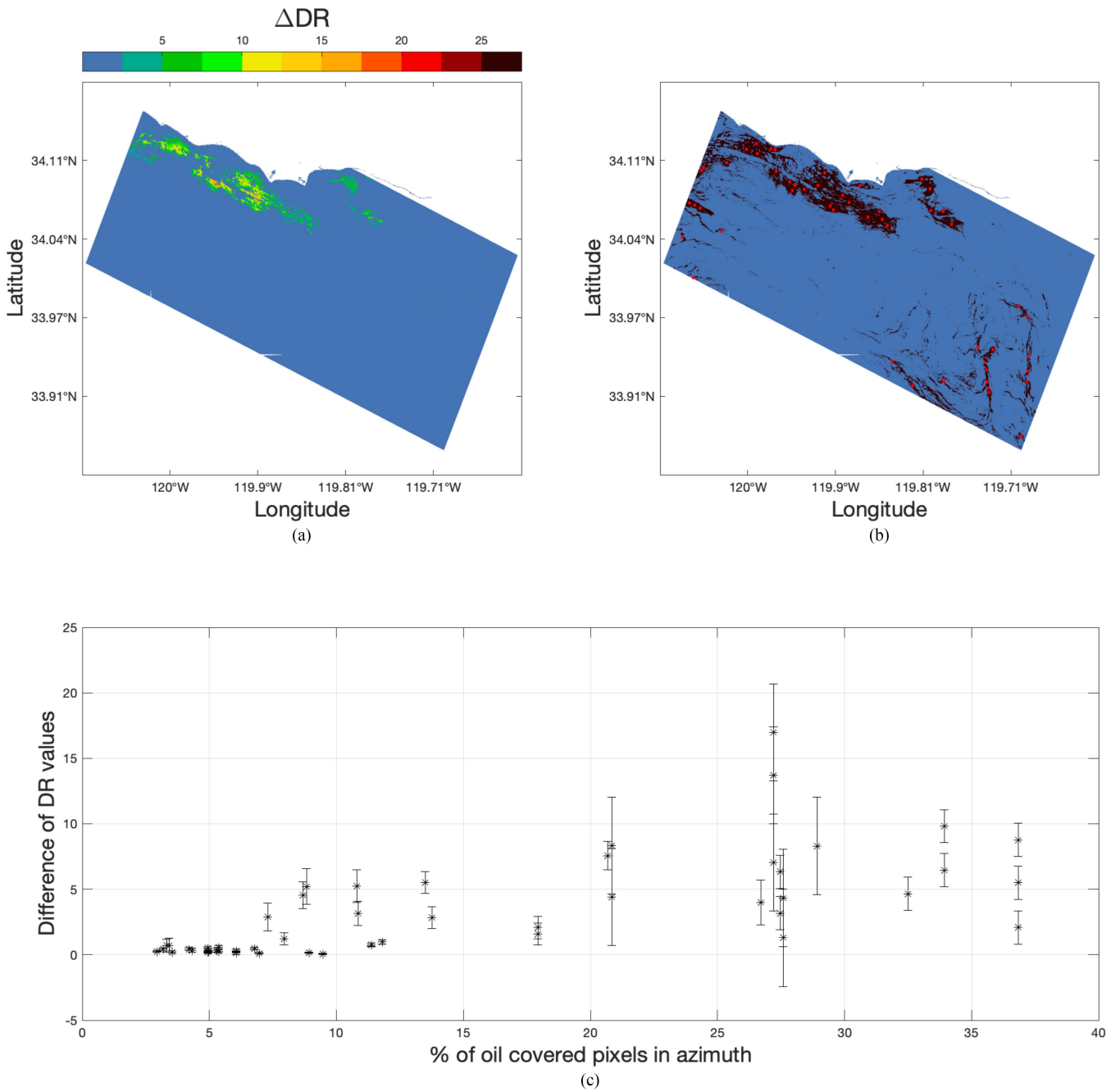

Fig. 10. (a) Image showing difference between retrieved DR values as calculated using the histogram method and median method. (b) Oil-water mask. Areas of oil slick delineated in black and open ocean in blue. Image was created by thresholding the UAVSAR data as seen in Fig. 4 at −24 dB. Red boxes in oil contaminated areas are 25 × 25 pixels ROIs. ROIs indicate areas in difference image (a) that are sampled. (c) Mean and standard deviation of each 25 × 25 pixel ROI from (a) plotted against the percentage of oil covered pixels in the azimuth direction.

red) are overlayed on an oil–water mask in Fig. 10(b), where areas in black indicate oil slicks and in blue, open water. The oil–water mask was generated by thresholding the UAVSAR image (VV polarimetric channel) at −24 dB. The mean and standard deviation for each of the ROIs were calculated and plotted against the percentage of pixels that contained oil for each incidence angle bin along the azimuth direction, as demonstrated in Fig. 10(c). The ROIs for which a small percentage of pixels are located within the oil slick for a given incidence angle bin showed a high degree of agreement between retrieved DR values for the two methods. When the percentage of oil covered pixels in azimuth was less than 7%, the mean difference values were close to zero with corresponding standard deviation values close to zero. The values begin to differ when more than 7% of pixels for a specific incidence angle bin are oil pixels.

This indicates that the median method, while computationally simple, can yield inconsistent values when there is even a relatively low percentage of oil pixels in the scene, particularly when clustered around a single angle of incidence.

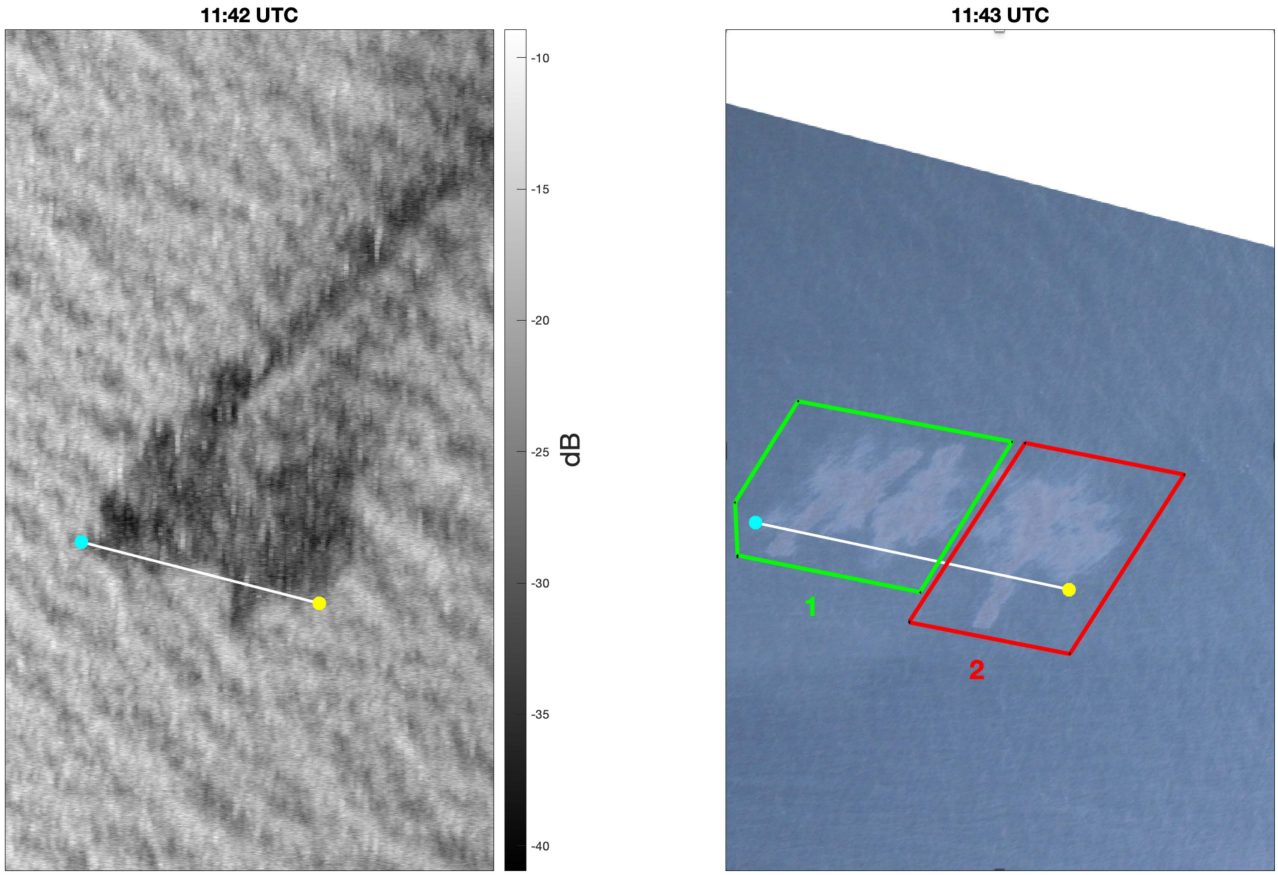

Fig. 11. (a) L-band F-SAR acquisition of mineral oil slick taken on June 12, 2019 at 11:42 UTC. The head of the slick is shown along with a portion of the tail. (b) Photograph of the same mineral oil slick taken from the Dornier DO228-212 aircraft carrying the F-SAR instrument at 11:43 UTC. Two zones are outlined by green and red boxes. The blue and yellow points connected with a white line indicate approximately the same positions in the two images. Photograph: Ralph Horn. Images published with permission from NOFO.

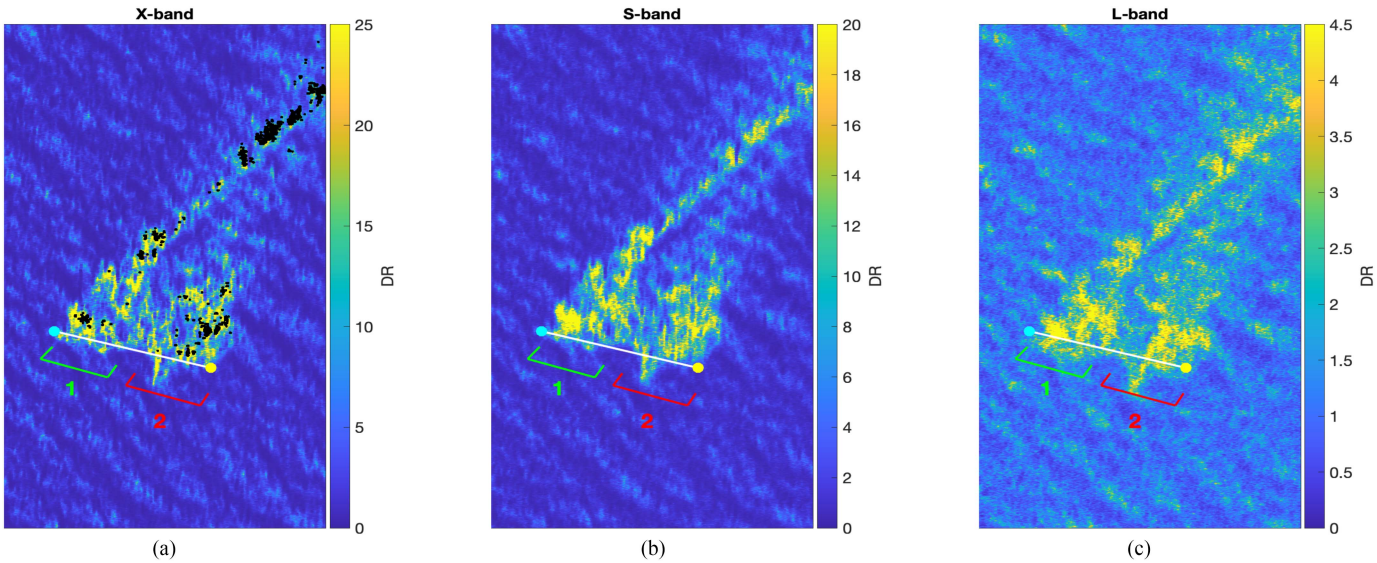

Fig. 12. (a)–(c) DR values calculated using the Histogram method for the slick shown in Fig. 11(a) for X-, S-, and L-bands. The black regions in (a) indicate pixels that are noise corrupted. Upper thresholds have been applied for better visualization. Areas that correspond to the oil slick zones, 1 and 2, in the optical image in Fig. 11(b) are indicated with a green and red bracket, respectively. The same blue and yellow points connected with a white line, which indicate the same relative positions between the SAR image and the photograph, are also shown.

TABLE III
AVERAGED DISTANCE MEASURES ($\langle d \rangle$) CALCULATED FROM DR VALUES WITHIN EACH BOUNDING BOX IN FIG. 5

	Strip Method	Random Sampling Method	Median Method	Histogram Method
$\langle d \rangle$	0.19	0.05	0.08	0.05

D. Comparison Between DR Values Derived for Different Scene Sizes

In this section, we compare the retrieved DR values computed for different scene sizes. This was achieved using the Sentinel-1 data that were introduced in Section IV-C and which is shown in Fig. 5. Different scene sizes are simulated using the red, green, and black bounding boxes around the oil slick (see Fig. 5). For the random sampling method, a mask was manually delineated to mask out oil slick and ship pixels. For the strip method, $\sigma_{TR}^{0,\text{sea}}(\theta)$ was calculated from the shaded regions directly below each bounding box.

For each of the four methods applied, we define a three-dimensional coordinate system (DR_{red}, DR_{gr}, DR_{bl}) whose coordinate axes are defined by DR values within the slick, calculated for each of the bounding boxes in Fig. 5, respectively. If the calculated within slick DR values are exactly equal for each scene size, the scatter of points in this space will lie exactly on the line defined by

$$\begin{bmatrix} \text{DR}_{\text{red}} \\ \text{DR}_{\text{gr}} \\ \text{DR}_{\text{bl}} \end{bmatrix} = t \begin{bmatrix} 1 \\ 1 \\ 1 \end{bmatrix} \quad \forall\, \text{t} \in [0, \infty)\,. \tag{2}$$

If the calculated DR values are not preserved when calculated using differing scene sizes, the point in this space, $(\text{dr}_{\text{red}}^i, \text{dr}_{\text{gr}}^i, \text{dr}_{\text{bl}}^i)$, for the ith within slick pixel will lie off this line and will have a perpendicular distance d to the line given as

$$d^i = \min \sqrt{\left(\text{DR}_{\text{red}} - \text{dr}_{\text{red}}^i\right)^2 + \left(\text{DR}_{\text{gr}} - \text{dr}_{\text{gr}}^i\right)^2 + \left(\text{DR}_{\text{bl}} - \text{dr}_{\text{bl}}^i\right)^2} \tag{3}$$

The averaged distance for all points is then expressed as

$$\langle d \rangle = \frac{\sum_1^n d^i}{n} \tag{4}$$

where n is the number of slick pixels. The averaged distance measures for all four methods are given in Table III.

By this measure, the strip method has the highest degree of variance between retrieved DR values for different scene sizes and the random sampling method and the histogram method have the least. This again indicates that the strip method has the drawback of producing varying numeric estimates for the DR when calculated for scenes with different spatial extents.

VI. COMPARISON BETWEEN SAR-DERIVED DR VALUES AND OPTICAL IMAGERY

Here, we compare histogram method DR values for the mineral oil slick for the X-, S-, and L-bands F-SAR acquisition taken during the NORSE 2019 oil-on-water exercise at 11:42 UTC (same as in Figs. 3(a) and 6) with a photograph taken 1 min later at 11:43 UTC [see Fig 11(b)]. Fig. 11(a) shows the S-band F-SAR acquisition of the head of the mineral oil slick, and a portion of the tail of the slick is also visible. Neither the SAR image nor the photograph are georeferenced. However, the photograph was skewed to roughly match the orientation of the SAR image. Two markers, one in blue and one in yellow connected with a white line, are inserted into both images to indicate the same relative positions. It should be noted that in the optical image in Fig. 11(b), the tail of the slick, as seen in the SAR image, is not visible. Fig. 3(b) shows a photograph of the same slick, shown in Fig. 11(b), but from an oblique viewing angle. As can be seen, the tail of the slick can be delineated. Two distinct zones within the head of the slick are outlined in Fig. 11(b): zone 1 (green box) and zone 2 (red box).

Fig. 12(a)–(c) shows the DR values for the X-, S-, and L-band acquisitions, respectively. Like findings in [4], [5], and [9], the DR values for S-band were higher than for L-band. However, unlike those findings, the X-band DR values were found to be lower than in S-band. One possible explanation for this is the noise contained within the X-band imagery. In [37], the L-band image was found to have significantly lower noise equivalent sigma zero (NESZ) values, -45 to 60 dB, than X- and S-bands, -30 to -45 dB. To evaluate the number of pixels primarily corrupted with noise in the X-, S-, and L-bands of the F-SAR acquisition and, following the work in [6] and [35], a 6 dB threshold above the noise floor was used to separate out pixels for further analysis. Only the X-band imagery was found to have pixels below this 6 dB limit, and these pixels are marked in black in Fig. 12(a). Thus, a better SNR might have resulted in higher DR values in the X-band data and, thus, keeping the X-band DR results in-line with previous measurements. It should be noted that upper thresholds have been applied to the DR values in Fig. 12(a)–(c). This is so the dynamic range of the DR values could be reduced so that comparisons could be made with the optical image in Fig. 11(b).

As can be seen in the S- and L-bands DR imagery in Fig. 12(b) and (c), zone 1 (green bracket) and zone 2 (red bracket), which are likewise delineated in the optical image in Fig. 11(b) via green and red boxes respectively, can be discerned. In the optical image [see Fig. 11(b)], a small gap with open water between zones 1 and 2 can be seen. This divide can likewise be discerned in the DR imagery in Fig. 12(b) and (c). In all three DR images [see Fig. 12(a)–(c)], a portion of the tail section has relatively high DR values, although this is not visible in the optical image. It should be noted that much of the DR values within zones 1 and 2 for X-band [see Fig. 12(a)] were affected by a low SNR. Despite this, the open water gap between zones 1 and 2 can still be seen but to a lesser extent than in the S- and L-bands DR.

VII. CONCLUSION

In this study, we examine four alternative methods to calculate the DR: the strip method, the random sampling method, the median method [29], and the histogram method [10], and compare these against each other using data from several sensors and radar frequencies. SAR-derived oil spill surveillance products based on the DR rely on accurately estimated DR values, especially when time-series data are employed. In addition, real-world oil

spill scenarios include complicated surface slick distributions with a variety of additional scattering targets present, such as land, ships, and oil rigs, thus complicating the extraction of a clean strip of open ocean pixels in the range direction. It should be noted that the DR provides a measure of contrast between open ocean and radar dark scattering targets, which include oil slicks but can also include look-alike phenomena such as biogenic slicks or low wind. Here, we apply the DR to scenes with only mineral oil slicks but note that further work can be done to separate look-alike phenomena, including the DR as one parameter.

We demonstrate that the method most often cited in the literature, the strip method, is not adequate to operationally estimate the DR. The random sampling method is intuitively simple but requires identifying and masking the oil pixels before being implemented. The median method is straightforward to implement and requires no information on oil slick distribution within a scene. The histogram method is the most computationally complex to implement but can be automated, is robust against outliers, and works even when relatively few open water pixels are available.

In this study, we applied the latter three methods to a unique multifrequency F-SAR dataset of a mineral oil slick discharged under favorable experimental conditions. Under these circumstances, we show that the three methods cited provide reasonably consistent results for relative thickness across all frequency bands and for thin and thick oil (i.e., the head and the tail of the mineral oil slick). As expected, differences in the spatial extent between the head of the mineral oil slick or the tail were not observed between methods as the DR measure performs a pixelwise transformation on the original SAR imagery.

Additionally, it was found that the histogram method and median method provide similar relative thickness information and the most similar numeric DR values, showing that these two methods, which rely on using all pixels within the scene, are the most consistent. Given that no masking is required and that scenes with more complicated slick geometries can be analyzed using these two methods, they are the most suitable for operational implementation since they can easily be fully automated.

However, for the median method, it was found that when a small percentage of oil pixels within an incidence angle bin was present (7% for the case of the UAVSAR scene in this study), the derived $\sigma_{TR}^{0,\text{sea}}(\theta)$ "clean ocean" values became noticeably biased toward lower values, thus indicating that the histogram method is more robust for large spills.

Our results show that the histogram method should be applied when calculating the DR for operational purposes. Although it requires more computation than the other methods, forming the histogram and identifying the clean water are simple computations, and it provides more consistent results, works on more complex scenes, and can be automatically applied to a SAR scene without any prior assessment of the slick's location.

As shown in this study, the S- and L-band derived DR values appeared to show the greatest visual correspondence with the aerial photograph both for identifying general areas of greater thickness and for correctly indicating zones of internal thickness variation within slick. The X-band derived DR values showed some degree of correspondence with the photograph but conclusions that can be drawn are limited due to noise corruption. Future work should aim to verify this using a larger suite of geolocated optical data acquired simultaneously with SAR imagery. Furthermore, the findings of this study could potentially be extended to other types of sensor data exhibiting statistical behavior similar to that of SAR. These sensors may include, but are not limited to, laser fluorosensors and infrared instruments. However, to confirm this, further investigation is required.

ACKNOWLEDGMENT

The authors would like to thank M. Espeseth from Kongsberg Satellite Services for her contributions to the preparation on this article. The authors also sincerely thank NOFO for including our experiment in their exercise. In particular, they would like to thank the crew from NOFO onboard R/V HH and K. K. Huseby at NOFO HQ for her efforts in accommodating their numerous requests. They would also like to thank DLR and the crew on board the F-SAR aircraft. UAVSAR data courtesy NASA/JPL-Caltech. UAVSAR data can be downloaded from uavsar.jpl.nasa.gov or from the Alaska Satellite Facility (http://www.asf.alaska.edu). They also wish to acknowledge the European Unions Earth observation program, Copernicus, for the use of Sentinel-1 data. Sentinel-1 data can be downloaded from https://scihub.copernicus.eu.

REFERENCES

[1] K. P. Singh, A. L. Gray, R. K. Hawkins, and R. A. O'Neil, "The influence of surface oil on C-and Ku-band ocean backscatter," *IEEE Trans. Geosci. Remote Sens.*, vol. GE-24, no. 5, pp. 738–744, Sep. 1986.

[2] Bonn Agreement Secretariat, Bonn Agreement Aerial Operations Handbook, Tech. Info. Paper, London, U.K., 2016, Accessed: Oct. 27, 2020. [Online]. Available: https://www.bonnagreement.org/site/assets/files/1081/aeriaa_operations_handbook.pdf

[3] M. Fingas and C. Brown, "Review of oil spill remote sensing," *Spill Sci. Techn. Bull.*, vol. 4, no. 4, pp. 199–208, 1997.

[4] M. Gade, W. Alpers, H. Hu¨hnerfuss, H. Masuko, and T. Kobayashi, "Imaging of biogenic and anthropogenic ocean surface films by the mul-tifrequency/multipolarization SIR-C/X-SAR," *J. Geophysical Res., Oceans*, vol. 103, no. C9, pp. 18851–18866, Aug. 1998.

[5] M. Gade, W. Alpers, H. Hu¨hnerfuss, V. Wismann, and P. Lange, "On the reduction of the radar backscatter by oceanic surface films: Scatterometer measurements and their theoretical interpretation," *Remote Sens. Environ.*, vol. 66, no. 1, pp. 52–70, Oct. 1998.

[6] B. Minchew, C. E. Jones, and B. Holt, "Polarimetric analysis of backscatter from the deepwater horizon oil spill using L-band synthetic aperture radar," *IEEE Trans. Geosci. Remote Sens.*, vol. 50, no. 10, pp. 3812–3830, Oct. 2012.

[7] B. Minchew, "Determining the mixing of oil and sea water using polarimetric synthetic aperture radar," *Geophysical Res. Lett.*, vol. 39, no. 16, pp. 1–6, Aug. 2012.

[8] C. E. Jones and B. Holt, "Experimental L-band airborne SAR for oil spill response at sea and in coastal waters," *Sensors*, vol. 18, no. 2, Feb. 2018, Art. no. 641.

[9] V. Wismann, M. Gade, W. Alpers, and H. Huhnerfuss, "Radar signatures of marine mineral oil spills measured by an airborne multi-frequency radar," *Int. J. Remote Sens.*, vol. 19, no. 18, pp. 3607–3623, Dec. 1998.

[10] C. E. Jones, "An automated algorithm for calculating the ocean contrast in support of oil spill response," *Mar. Pollut. Bull.*, vol. 191, Jun. 2023, Art. no. 114952.

[11] M. M. Espeseth, C. E. Jones, B. Holt, C. Brekke, and S. Skrunes, "Oil-spill-response-oriented information products derived from a rapid-repeat time series of SAR images," *IEEE J. Sel. Topics Appl. Earth Observ. Remote Sens.*, vol. 13, pp. 3448–3461, 2020.

[12] W. Alpers and H. Hu¨hnerfuss, "Radar signatures of oil films floating on the sea surface and the Marangoni effect," *J. Geophysical Res., Oceans*, vol. 93, no. C4, pp. 3642–3648, Apr. 1988.
[13] A. D. Jenkins and S. J. Jacobs, "Wave damping by a thin layer of viscous fluid," *Phys. Fluids*, vol. 9, no. 5, pp. 1256–1264, May 1997.
[14] N. Pinel, C. Bourlier, and I. Sergievskaya, "Two-dimensional radar backscattering modeling of oil slicks at sea based on the model of local balance: Validation of two asymptotic techniques for thick films," *IEEE Trans. Geosci. Remote Sens.*, vol. 52, no. 5, pp. 2326–2337, May 2014.
[15] Y. Zhang, J. Zhang, Y. Wang, J. Meng, and X. Zhang, "The damping model for sea waves covered by oil films of a finite thickness," *Acta Oceanologica Sinica*, vol. 34, no. 9, pp. 71–77, Nov. 2014.
[16] T. Meng, F. Nunziata, A. Buono, X. Yang, and M. Migliaccio, "On the joint use of scattering and damping models to predict X-band co-polarized backscattering from a slick-covered sea surface," *Front. Mar. Sci.*, vol. 9, Dec. 2022, Art. no. 1113068.
[17] I. Sergievskaya, S. Ermakov, T. Lazareva, and J. Guo, "Damping of surface waves due to crude oil/oil emulsion films on water," *Mar. Pollut. Bull.*, vol. 146, pp. 206–214, Sep. 2019.
[18] H. Zheng, J. Zhang, Y. Zhang, A. Khenchaf, and Y. Wang, "Theoretical study on microwave scattering mechanisms of sea surfaces covered with and without oil film for incidence angle smaller than 30°," *IEEE Trans. Geosci. Remote Sens.*, vol. 59, no. 1, pp. 37–46, Sep. 2021.
[19] W. Alpers and H. Hu¨hnerfuss, "The damping of ocean waves by surface films: A new look at an old problem," *J. Geophysical Res., Oceans*, vol. 94, no. C5, pp. 6251–6265, 1989.
[20] M. W. Hansen, V. Kudryavtsev, B. Chapron, C. Brekke, and J. A. Johannessen, "Wave breaking in slicks: Impacts on C-band quad- polarized SAR measurements," *IEEE J. Sel. Topics Appl. Earth Observ. Remote Sens.*, vol. 9, no. 11, pp. 4929–4940, Nov. 2016.
[21] C.-S. Yang, S.-M. Park, Y. Oh, and K. Ouchi, "An analysis of the radar backscatter from oil-covered sea surfaces using moment method and Monte-Carlo simulation: Preliminary results," *Acta Oceanologica Sinica*, vol. 32, no. 1, pp. 59–67, Jan. 2013.
[22] G. Franceschetti, A. Iodice, D. Riccio, G. Ruello, and R. Siviero, "SAR raw signal simulation of oil slicks in ocean environments," *IEEE Trans. Geosci. Remote Sens.*, vol. 40, no. 9, pp. 1935–1949, Sep. 2002.
[23] D. Latini, F. Del Frate, and C. E. Jones, "Multi-frequency and polarimetric quantitative analysis of the Gulf of Mexico oil spill event comparing different SAR systems," *Remote Sens. Environ.*, vol. 183, pp. 26–42, Sep. 2016.
[24] S. Skrunes, C. Brekke, C. Jones, M. Espeseth, and B. Holt, "Effect of wind direction and incidence angle and polarimetric SAR observations of slicked and unslicked surfaces," *Remote Sens. Environ.*, vol. 213, pp. 73–91, 2018.
[25] O. Garcia-Pineda et al., "Classification of oil spill by thicknesses using multiple remote sensors," *Remote Sens. Environ.*, vol. 236, Jan. 2020, Art. no. 111421.
[26] D.-J. Kim, W. M. Moon, and Y.-S. Kim, "Application of TerraSAR-X data for emergent oil-spill monitoring," *IEEE Trans. Geosci. Remote Sens.*, vol. 48, no. 2, pp. 852–863, Feb. 2010.
[27] S. Skrunes, A. M. Johansson, and C. Brekke, "Synthetic aperture radar remote sensing of operational platform produced water releases," *Remote Sens.*, vol. 11, 2019, Art. no. 2882.
[28] C. E. Jones, M. M. Espeseth, and A. M. Johansson, private communication, Nov. 2021.
[29] M. M. Espeseth, "Analysis of oil spill and sea ice measurements using full-polarimetric and hybrid-polarity synthetic aperture radar data," Ph.D. dissertation, Dept. Phys. Tech., UiT—Arctic Univ. of Norway, Tromsø, Norway, 2019. [Online]. Available: https://hdl.handle.net/10037/16973
[30] C. Brekke, M. M. Espeseth, K. F. Dagestad, J. Röhrs, L. R. Hole, and A. Reigber, "Integrated analysis of multisensor datasets and oil drift simulations - A free-floating oil experiment in the open ocean," *J. Geophysical Res., Oceans*, vol. 126, no. 1, Jan. 2021, Art. no. e2020JC016499.
[31] A. Reigber et al., "Performance of the P- band subsystem and the X-band interferometer of the F-SAR airborne SAR instrument," in *Proc. IEEE Int. Geosci. Remote Sens. Symp.* , Jul. 2012, pp. 5037–5040.
[32] A. G. Fore et al., "UAVSAR polarimetric calibration," *IEEE Trans. Geosci. Remote Sens.*, vol. 53, no. 6, pp. 3481–3491, Jun. 2015.
[33] M. Bourbigot et al., "Sentinel-1 product definition," Tech. Info. Paper, 2016, Accessed on: May 14, 2023. [Online]. Available: https://sentinels.copernicus.eu/documents/247904/1877131/Sentinel-1-Product-Definition.pdf/6049ee42-6dc7-4e76-9886-f7a72f5631f3?t=1461673251000
[34] C. E. Jones et al., "Measurement and modeling of oil slick transport," *J. Geophysical Res., Oceans*, vol. 121, no. 10, pp. 7759–7775, Oct. 2016.
[35] A. Freeman and S. Durden, "A three-component scattering model for polarimetric SAR data," *IEEE Trans. Geosci. Remote Sens.*, vol. 36, no. 3, pp. 963–973, May 1998.
[36] G. R. Valenzuela, "Scattering of electromagnetic waves from a tilted slightly rough surface," *Radio Sci.*, vol. 3, no. 11, pp. 1057–1066, Jan. 1968.
[37] C. Quigley, C. Brekke, and T. Eltoft, "Comparison between dielectric inversion results from synthetic aperture radar co- and quad-polarimetric data via a polarimetric two scale model," *IEEE Trans. Geosci. Remote Sens.*, vol. 60, 2022, Art no. 4200218.

Cornelius Quigley received the bachelor's degree in physics in June 2013 from the Department of Physics, National University of Ireland, Cork, Ireland, the master's degree in sea ice remote sensing using SAR from the Department of Physics and Technology, UiT—The Arctic University of Norway, Tromsø, Norway, in June 2017, and the Ph.D. degree in oil spill remote sensing using SAR from the Center for Integrated Remote Sensing and Forecasting for Arctic Operations, UiT—The Arctic University of Norway, Tromsø, in March 2021.

His current research interests include remote sensing of ocean areas, specifically by polarimetric SAR, and with a focus on marine oil pollution.

A. Malin Johansson (Member, IEEE) received the M.Sc. degree in physical oceanography from Gothenburg University, Gothenburg, Sweden, in 2005, and the Ph.D. degree in remote sensing from Stockholm University, Stockholm, Sweden, in 2012.

She is an Associate Professor with the Department of Physics and Technology, UiT The Arctic University of Norway, Tromsø, Norway, which she jointed in 2014. She was a Postdoctoral Researcher with the Radar Remote Sensing Group, Department of Earth and Space Sciences, Chalmers University of Technology, Gothenburg, Sweden. Her research interests include multisensor remote sensing of sea ice, oil spills, and harmful algae blooms.

Cathleen E. Jones (Member, IEEE) received the B.S. degree from Texas A&M University, College Station, TX, USA, in 1982, and the Ph.D. degree from the California Institute of Technology, Pasadena, CA, USA, in 1991, both in physics.

She is a Senior Research Scientist with the NASA Jet Propulsion Laboratory, California Institute of Technology, where her main research is focused on development of methods for determining oil slick characteristics, monitoring subsidence and critical infrastructure, and understanding land building/loss in deltas. She is the Applications Co-Lead of the NASA NISAR Science Team.